

# Water and bottom properties of a coastal environment derived from Hyperion data measured from the EO-1 spacecraft platform

ZhongPing Lee<sup>a</sup>, Brandon Casey<sup>b</sup>, Robert Arnone<sup>a</sup>, Alan Weidemann<sup>a</sup>,  
Rost Parsons<sup>c</sup>, Marcos J. Montes<sup>d</sup>, Bo-Cai Gao<sup>d</sup>, Wesley Goode<sup>a</sup>,  
Curtiss O. Davis<sup>e</sup>, Julie Dye<sup>f</sup>

<sup>a</sup>Naval Research Laboratory, Code 7333  
Stennis Space Center, MS 39529

[zplee@nrlssc.navy.mil](mailto:zplee@nrlssc.navy.mil)

<sup>b</sup>Planning Systems, Inc.

Stennis Space Center, MS 39529

<sup>c</sup>NOAA\NESDIS\NCDDC

Stennis Space Center, MS 39529

<sup>d</sup>Naval Research Laboratory, Code 7232

Washington, DC 20375

<sup>e</sup>College of Oceanic and Atmospheric Sciences

Oregon State University

Corvallis, OR 97331-5503

<sup>f</sup>NAVOCEANO, Code NP2

Stennis Space Center, MS 39529

**Abstract.** Hyperion is a hyperspectral sensor on board NASA's EO-1 satellite with a spatial resolution of approximately 30 m and a swath width of about 7 km. It was originally designed for land applications, but its unique spectral configuration (430 nm – 2400 nm with a ~10 nm spectral resolution) and high spatial resolution make it attractive for studying complex coastal ecosystems, which require such a sensor for accurate retrieval of environmental properties. In this paper, Hyperion data over an area of the Florida Keys is used to develop and test algorithms for atmospheric correction and for retrieval of subsurface properties. Remotesensing reflectance derived from Hyperion data is compared with those from *in situ* measurements. Furthermore, water's absorption coefficients and bathymetry derived from Hyperion imagery are compared with sample measurements and LIDAR survey, respectively. For a depth range of ~ 1 – 25 m, the Hyperion bathymetry match LIDAR data very well (~11% average error); while the absorption coefficients differ by ~16.5% (in a range of 0.04 – 0.7 m<sup>-1</sup> for wavelengths of 410, 440, 490, 510, and 530 nm) on average. More importantly, in this top-to-bottom processing of Hyperion imagery, there is no use of any *a priori* or ground truth information. The results demonstrate the usefulness of such space-borne hyperspectral data and the techniques developed for effective and repetitive observation of complex coastal regions.

**Keywords:** aquatic environment, satellite, remote sensing, bathymetry, LIDAR.

## 1 INTRODUCTION

Coastal and estuarine regions are important parts of the coastal ecosystem. They are not only the productive water that support the fishery industry, but also are more directly related to human activities via recreation. However, as a result of population expansion and economic development as well as a variety of natural events, many coastal areas have suffered shoreline erosions, declines in aquatic species, losses in seagrass beds, and bleaching of coral reefs [e.g.,

1, 2]. Eutrophication and sediment resuspension contribute to the deterioration of water clarity that leads to change of ecosystems, whereas shoreline erosion and redeposition alter coastal navigations. Such changes demand efficient and reliable updating of its status.

The traditional bathymetry and water property monitoring technique requires frequent ship surveys. While this kind of observation can provide detailed information about the chosen sites, it cannot show what happens to the broader coastal environment, and may miss places of dramatic change. To document the properties of the broad coastal environment instead of a few chosen sites, repetitive measurements by satellite sensors offer an attractive alternative. However, to adequately monitor complex coastal environments [3] via ocean color radiometry (OCR) requires not only sophisticated sensors but also advanced data processing algorithms [4].

For shallow coastal waters, Lee and Carder [5] have demonstrated that reliable derivation of water and bottom properties from spectral remote sensing requires a sensor with hyperspectral capability. Current operational satellite sensors designed for observation of biogeochemical properties of the global ocean, such as SeaWiFS or MODIS, have only about 8 spectral bands in the visible-infrared domain and a large spatial footprint (~1 km). Such sensors can provide valuable observations on properties of the open ocean, but they cannot provide the detailed spectral and spatial information needed for shallow coastal environments.

The Hyperion sensor on board NASA's EO-1 platform [6] has more than 200 channels covering ~430 nm to 2400 nm and a ground resolution of about 30 m (for nadir viewing). Hyperion was designed for bright land targets and it has a marginal Signal-to-Noise Ratio (SNR) for dark ocean targets. Its spectral and spatial characteristics, however, are significantly better suited for the study of coastal waters than sensors such as SeaWiFS or MODIS.

The SNR of Hyperion is typically in the range of 50 – 150, whereas the SNR of SeaWiFS or MODIS are around or better than 500. The low SNR has a large impact on water observation. Water targets typically have much weaker signal than land targets. Thus Hyperion may not have enough sensitivity to differentiate the subtle change of water properties. Consequently it has been perceived that Hyperion would have little usefulness for water observations. On the other hand, for many shallow coastal areas, due to the increased turbidity of water, and in places with strong reflectance from the bottom, the signals emanating from the water surface can be much stronger than that from open ocean waters. An earlier study by Brando and Dekker [7] of Hyperion data over Moreton Bay (Australia) clearly demonstrated that Hyperion imagery could be very useful in mapping water properties of coastal areas. That study, however, was focused on the properties of the water column (such as concentrations of chlorophyll and suspended particles, and absorption of yellow substance); and utilized only Hyperion-collected spectral information at 490 nm, 670 nm, and the average in the range of 700 – 740 nm. Also, similar to the traditional standard strategy, the atmospheric correction in Brando and Dekker [7] requires that both the sensor and the atmosphere model provide accurate top-of-atmosphere (TOA) spectral radiance ( $L_t(\lambda)$ ).  $\lambda$  is the wavelength in air and is omitted in the remainder of the text for brevity unless needed for clarification.) in order to obtain reliable water-leaving radiance ( $L_w$ ). Unfortunately the radiometric accuracy of  $L_t$  is only about  $\pm 5\%$  for Hyperion [8], which may cause significant errors in  $L_w$  because  $L_w$  is generally no more than 10-20% of  $L_t$  [9].

In this study, using Hyperion data collected over the Florida Keys as an example, we present a practical image-driven method for correcting the effects of atmosphere for such sensors. Furthermore, the corrected signal (remote-sensing reflectance of water) is fed into a hyperspectral optimization processing scheme [10, 11] to derive properties of the water column and the bottom. Hyperion derived results are then compared with *in situ* and LIDAR measurements, respectively, to evaluate the performances of the methods. The excellent agreement demonstrates that hyperspectral data, even from sensors such as Hyperion with low SNR, when used with this innovative method for atmosphere correction and the advanced

algorithm for retrieval of environmental properties, can provide reliable and useful information for effective monitoring of coastal ecosystems.

## 2 DATA

Level 1 Hyperion data over Looe Key (Florida) collected on October 26, 2002 was provided by the USGS. Because our focus is on water and bottom properties, only spectral information in the range of 428 – 925 nm was used. The image was centered at 24°42'39" (N), 81°22'15" (W). Figure 1 presents the full scene (before georeferencing) of this Hyperion collection. This image covers clear oceanic waters, shallow waters with varying bottom reflectivity, and complex out flows from nearby coasts. For this study, data analysis was focused on the sub-scene (~ 140 km<sup>2</sup>, see Fig. 1, right) that overlaps most with available LIDAR bathymetry.

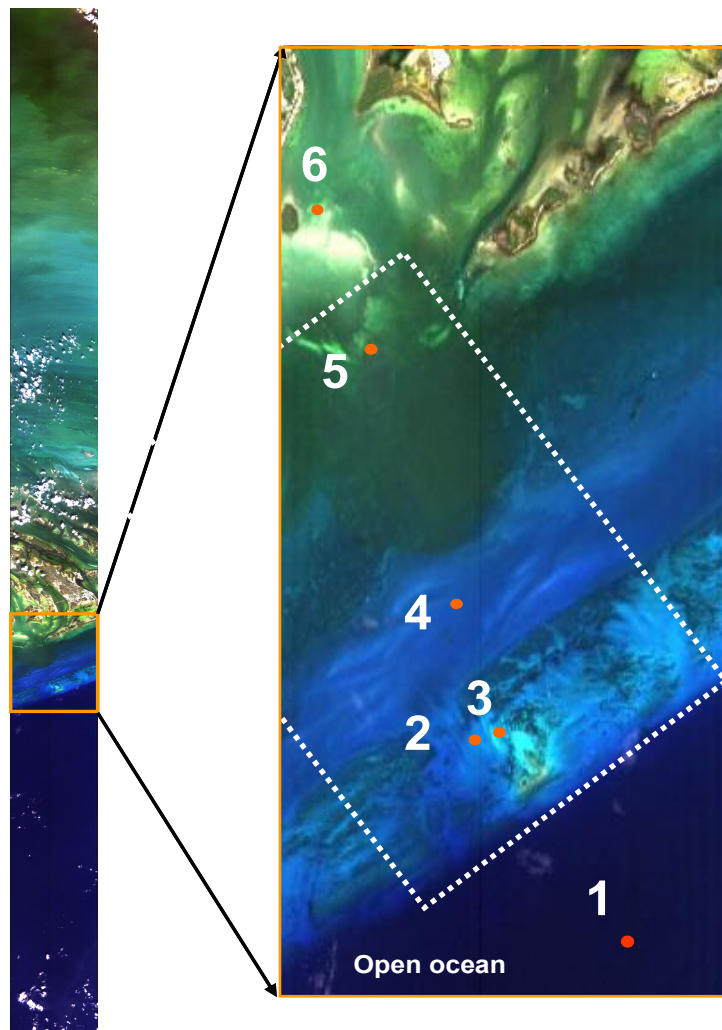


Fig. 1. Hyperion collection (October 26, 2002) over the Florida Keys (before georeferencing). Left is the full scene; right is a subset that has both *in situ* and LIDAR measurements (within the dashed box). Numbers in the subset indicate the locations of the six stations with *in situ* measurements.

During the collection of Hyperion data, *in situ* measurements of remote-sensing reflectance ( $R_{rs}$ , which is defined as ratio of water-leaving radiance ( $L_w$ ) to downwelling irradiance just above the surface ( $E_d$ )) and water optical properties were also carried out at six sites in the area (red dots in Fig. 1). Remote-sensing reflectance was measured using a custom-made hand-held spectroradiometer [12] and water absorption coefficients were measured with an AC-9 (Wetlabs, Inc., Philomath, OR). All measurements and data processing followed the NASA protocols [13]. During the measurements, the sea state was quite calm with a wave height  $\sim 10$  cm.

Bathymetry was also collected using the SHOALS (Scanning Hydrographic Operational Airborne Lidar Survey, <http://shoals.sam.usace.army.mil>) system (but not exactly in the same footprint). This system is an earlier version of CHARTS (Compact Hydrographic Airborne Rapid Total Survey; NAVOCEANO), which is a survey system that includes hyperspectral and topographic/hydrographic LIDAR. SHOALS probes the water with a 532 nm YAG laser and uses the time difference between the surface return and the bottom return to measure the bottom depth. For the Looe Key area, two surveys were collected using SHOALS but with slightly different ground coverage. One was obtained the same day as the Hyperion image, the other on December 10, 2004. To increase the area of overlapping coverage between Hyperion and SHOALS data, the two LIDAR bathymetry data sets were combined to form one image after no significant variations were found between the two. A 0.75 m subtraction was made to the 2004 data to account for the tidal difference and to have a smooth transition at the survey boundaries. To account for the tidal effects between the merged LIDAR set and the Hyperion data, 0.2 m was subtracted from the merged LIDAR bathymetry prior to comparison with that from Hyperion (see section 5).

### 3 IMAGE-DRIVEN METHOD TO CORRECT ATMOSPHERIC EFFECTS

To analytically derive water and/or bottom properties from any satellite ocean-color data, the first step is to get high-quality spectral remote-sensing reflectance ( $R_{rs}$ ). It is  $R_{rs}$  that contains water and/or bottom information.

In general, the radiance measured by a sensor at any altitude ( $L_t$ ) can be expressed as

$$L_t(\lambda) = L_a(\lambda) + t(\lambda) L_w(\lambda), \quad (1)$$

with  $L_a$  representing contributions from the atmosphere and sea-surface reflectance, and  $L_w$  for contributions from below the water surface.  $t$  is the transmittance of  $L_w$  from sea surface to sensor altitude. From Eq. 1 and the definition of  $R_{rs}$ , we obtain

$$R_{rs}(\lambda) = \frac{L_t(\lambda) - L_a(\lambda)}{t(\lambda) E_d(\lambda)}. \quad (2)$$

To obtain  $R_{rs}$  from  $L_t$ , values of  $L_a$ ,  $t$ , and  $E_d$  must be known. Conventionally, standard approaches calculate values of  $L_a$ ,  $t$ , and  $E_d$  based on models of radiative transfer for the atmosphere [9, 14, 15], with the assumption that  $L_t$  is measured with high accuracy both spectrally and radiometrically. Since  $L_w$  in general makes up  $<20\%$  of  $L_t$ , such methods require extremely high accuracy (within  $\pm 1\%$  for ocean applications) in the measurement of  $L_t$  and high accuracy in the aerosol models. The Hyperion sensor, however, has a radiometric accuracy of only  $\pm 5\%$  in the measured  $L_t$  [8]. Such an uncertainty in  $L_t$  may cause a 50% error in  $L_w$  by the standard approach even with a perfect atmospheric model. Such large errors in turn can cascade into significant uncertainties in the derived water and/or bottom properties. As evidenced in Brando and Dekker [7] (their Fig. 2), the derived reflectance shows

significant non-smoothness even after spatial average [7], although the relative error was not large and water properties were derived reasonably well in that study.

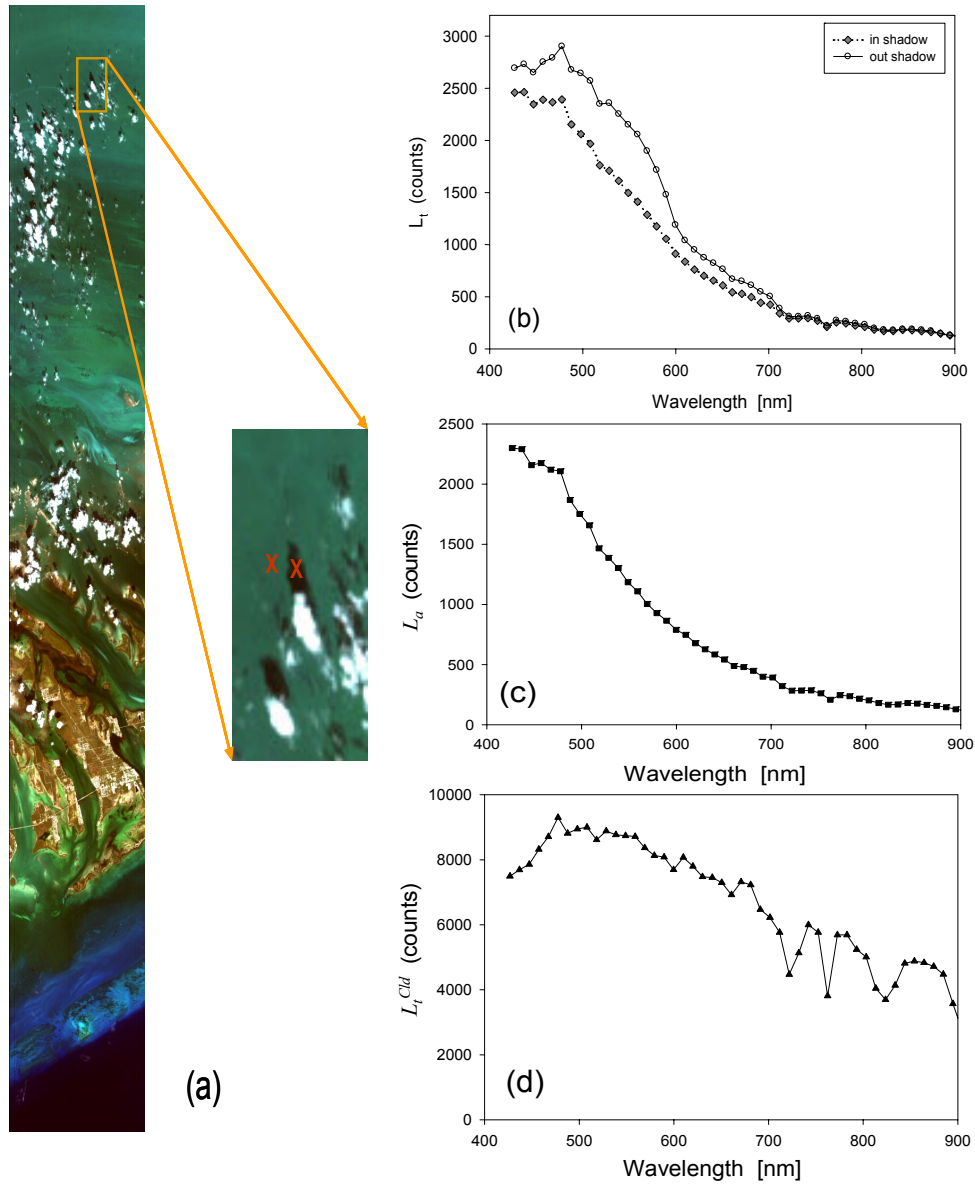


Fig. 2. (a) Pixels under the Sun and in the shadow used for correction of atmospheric effects. (b) The TOA radiance in raw counts of the two adjacent pixels under the Sun and clouds. (c) Derived atmospheric contribution to the TOA radiance after using the Cloud-Shadow method (see text for details). (d). Averaged TOA radiance of selected clouds.

To overcome the imperfect radiometric accuracy in Hyperion  $L_t$ , we applied a practical image-driven technique to correct the atmospheric contribution. This technique is an extension of the cloud-shadow method developed by Reinersman et al. [16]. In that method

[16],  $L_a$  is calculated from a pair of adjacent pixels that are in and out of a cloud shadow, with  $t$  and  $E_d$  calculated separately from a radiative transfer model after deriving aerosol properties. Therefore it does require the sensor to be well calibrated radiometrically and spectrally in order to match the calculated  $t$  and  $E_d$ .

In our adjusted approach, we calculated  $L_a$  in a similar but simplified fashion to that of Reinersman et al. [16], but  $t$  and  $E_d$  were evaluated differently. Specifically, 1)  $t$  and  $E_d$  were not explicitly derived separately; and 2) the product of  $t$  and  $E_d$  was estimated using the reflected radiance from the top of clouds.

Mathematically, for a pixel outside the shadow (under the Sun), its radiance ( $L_t^{Sun}$ ) can be expressed as,

$$L_t^{Sun}(\lambda) = L_a^{Sun}(\lambda) + t(\lambda) E_d(\lambda) R_{rs}(\lambda), \quad (3)$$

with  $E_d$  including contributions from both the Sun and sky [17]. For an adjacent pixel in the shadow that has the same water properties as that under the Sun, its radiance,  $L_t^{Sdw}$ , is given by,

$$L_t^{Sdw}(\lambda) = L_a^{Sdw}(\lambda) + t(\lambda) E_d^{Sky}(\lambda) R_{rs}(\lambda). \quad (4)$$

The  $R_{rs}$  under the Sun and in the shadow are actually slightly (<5%) different because of the different illuminations [18-21] even when they have the same water and bottom properties. This little difference is ignored here, however.

As an example, Figure 2a shows the locations of a pair of adjacent Sun-shadow pixels, while Figure 2b presents their corresponding TOA radiances (in raw counts).

Assume that  $L_a^{Sun} = L_a^{Sdw} = L_a$ , then the following is derived from Eqs. 3 and 4,

$$L_a(\lambda) = L_t^{Sun}(\lambda) - \frac{L_t^{Sun}(\lambda) - L_t^{Sdw}(\lambda)}{1 - E_d^{Sky}(\lambda)/E_d(\lambda)}. \quad (5)$$

Because  $E_d^{Sky}/E_d$  can be estimated from Radtran [17] for a given location and at a given time,  $L_a$  is then easily calculated from Eq. 5. Figure 2c presents the calculated  $L_a$  of the selected Sun-shadow pair, which is in the same units as  $L_t$  from the sensor (either in raw counts or absolute radiance). The values of  $E_d^{Sky}/E_d$  depend on atmospheric conditions (such as visibility, ozone depth, etc). However, in the process of deriving  $L_a$  here, because  $E_d^{Sky}/E_d$  is applied on the difference between  $L_t^{Sun}$  and  $L_t^{Sdw}$ , and this difference is significantly smaller than  $L_t^{Sun}$ , errors in  $E_d^{Sky}/E_d$  have only very limited effects on  $L_a$ . For instance, when  $E_d^{Sky}/E_d$  were calculated separately with the visibility values of 15 km and 30 km and resulted in ~30% difference in  $E_d^{Sky}/E_d$  for the blue wavelengths, the maximum difference in derived  $L_a$  was ~1%. Because of such negligible effects,  $E_d^{Sky}/E_d$  of the Sun-shadow pixels were calculated with the default atmospheric parameters in Radtran.

In this process of deriving  $L_a$ , it is more important to avoid sun glint that could contribute to  $L_t^{Sun}$  but not to  $L_t^{Sdw}$ . This could be carried out by choosing pixel pairs with no, or negligible, sun glint as we did here where the sun zenith angle was about 45° and the sensor was nadir looking. One could also correct for sun glint first [22] before deriving  $L_a$ . To test

the robustness of our process, another two pairs of adjacent Sun-shadow pixels from different locations with different water properties were selected and  $L_a$  calculated. The results (not shown here) were nearly identical to that shown here. Such results validate the calculation process and the assumption that  $L_a$  for this study was nearly uniform spatially.

To calculate  $R_{rs}$ , the product of  $tE_d$  is needed. For this component, we used the radiance measured over the clouds to make the estimation. If we assume that the atmospheric contribution is nearly uniform over the study area, the TOA radiance above a cloud is approximated as

$$L_t^{Cld}(\lambda) = L_a(\lambda) + t(\lambda) E_d(\lambda) \rho, \quad (6)$$

where  $\rho$  is the remote-sensing reflectance of the observed clouds. The  $\rho$  value corresponds to the spectrum of  $L_t^{Cld}$ , and is considered independent of wavelength based on measurements made in the visible-infrared domain [23, 24]. Figure 2d shows averaged  $L_t^{Cld}$  of a few selected clouds.  $R_{rs}$  at any pixel was then calculated from

$$R_{rs}(\lambda) = \rho \frac{L_t(\lambda) - L_a(\lambda)}{L_t^{Cld}(\lambda) - L_a(\lambda)}. \quad (7)$$

The value of  $\rho$  was determined from a clear water pixel by assuming  $R_{rs}(550 \text{ nm})$  value of  $0.002 \text{ sr}^{-1}$  [25], and a  $\rho$  value of  $\sim 0.16 \text{ sr}^{-1}$  was obtained for the averaged  $L_t^{Cld}$  of this study. For other Hyperion images, an effective  $\rho$  value could be obtained by comparing its  $L_t^{Cld}$  to the  $L_t^{Cld}$  used in this study.

To account for any residual contributions from the sky and the sea surface, a spectrally constant value was removed from the above calculated  $R_{rs}$  in order to obtain an average of zero for the spectral range of 810 - 840 nm, where contributions from water are considered null [26]. After these steps,  $R_{rs}$  of the entire Hyperion scene were derived. Figure 3 compares spectra of  $R_{rs}$  derived from Hyperion to those from *in situ* measurements. Excellent agreement, in both spectral shapes and spectral values, between the Hyperion  $R_{rs}$  and the *in situ*  $R_{rs}$  are obtained in four out of the six *in situ* stations. Note that these spectral  $R_{rs}$  varied widely from station to station. However, for two stations (St.2 and St.5), while the spectral shapes of the two  $R_{rs}$  spectra are quite consistent, respectively, the Hyperion  $R_{rs}$  are significantly higher than *in situ*  $R_{rs}$  in values. The reason for this mismatch is not absolutely certain but the *in situ* measurements suggest that pixels had different water-bottom properties. Note that the water or bottom properties were not uniform in those areas.

One obvious advantage of this image-driven approach to derive spectral  $R_{rs}$  is that  $L_t$ ,  $L_a$  and  $L_t^{Cld}$  come from the same sensor with all  $L_t$  components collected nearly simultaneously. Hence the derivation of  $R_{rs}$  does not depend on the absolute radiance value of  $L_t$ , because the sensor's response function (calibration factor) is canceled out. This can be extremely useful for sensors that are imperfectly calibrated or decay with time in uncontrollable and unknown fashions. Also, since  $L_a$  is in general the smaller spectrum of the image, it will be rare that  $R_{rs}$  calculated by this approach be negative in the visible domain. This method, however, does require a pair of adjacent Sun-shadow pixels with uniform surface properties, and this shadow cannot be from thin clouds. Also, it does depend on the assumption that  $L_a$  is nearly uniform for the study area. Such an assumption could be more problematic if the area under study is quite wide (hundreds of kilometers), as  $L_a$  is a function of many parameters that include aerosol load, solar zenith angle, and relative azimuth angle, etc.

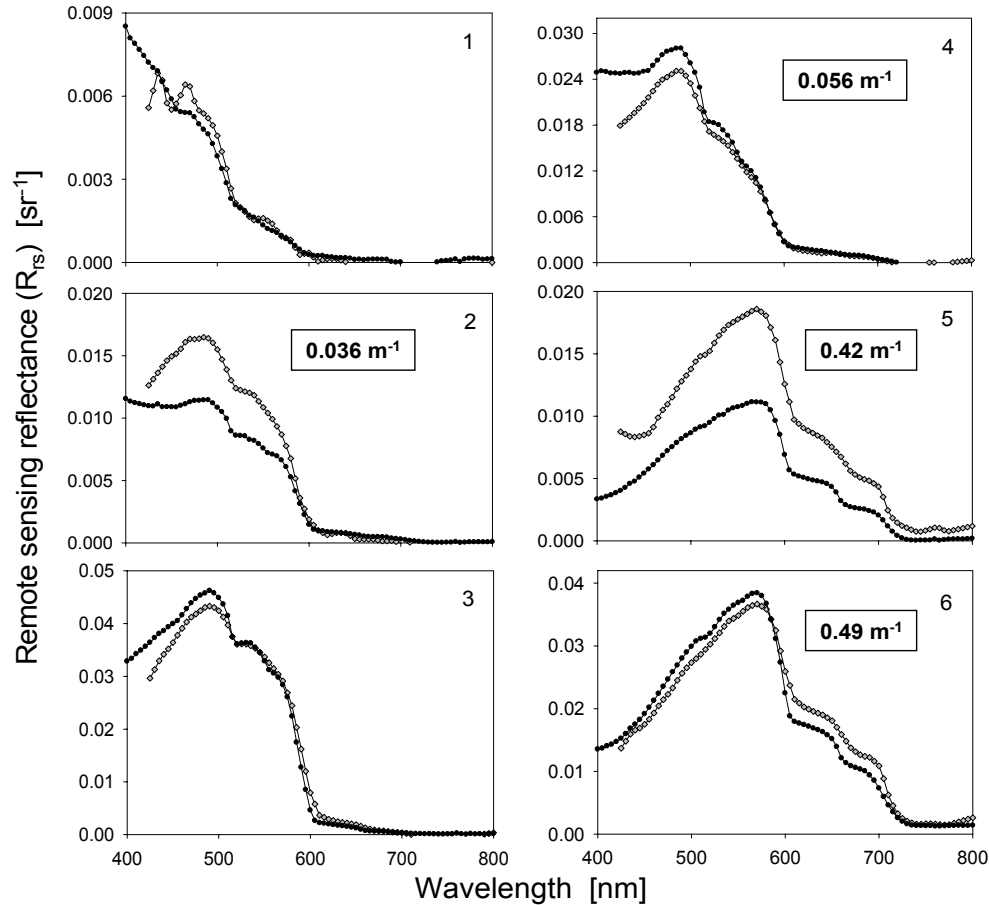


Fig. 3. Derived remote-sensing reflectance from Hyperion measurements (open symbol) and its comparison with that from *in situ* measurements (solid symbol). Numbers in the boxes indicate total absorption coefficients at 440 nm measured by an AC-9 (Wetlabs, Inc.).

#### 4 RETRIEVAL OF BOTTOM AND WATER COLUMN PROPERTIES

To derive properties of the water column and bottom from  $R_{rs}$ , we applied the spectral optimization approach developed by Lee et al. [10, 11]. Briefly, the approach analytically models  $R_{rs}$  spectrum as a function of five independent variables (representing properties of water column and bottom) for optically shallow waters, i.e.,

$$\begin{aligned}
 R_{rs}(\lambda_1) &= F(a_w(\lambda_1), b_{bw}(\lambda_1), \mathbf{P}, \mathbf{G}, \mathbf{X}, \mathbf{B}, \mathbf{H}) \\
 R_{rs}(\lambda_2) &= F(a_w(\lambda_2), b_{bw}(\lambda_2), \mathbf{P}, \mathbf{G}, \mathbf{X}, \mathbf{B}, \mathbf{H}) \\
 &\vdots \\
 R_{rs}(\lambda_n) &= F(a_w(\lambda_n), b_{bw}(\lambda_n), \mathbf{P}, \mathbf{G}, \mathbf{X}, \mathbf{B}, \mathbf{H})
 \end{aligned} \tag{8}$$

Here  $a_w$  and  $b_{bw}$  are the absorption and backscattering coefficients of pure seawater, with values taken from the literature [27, 28] and considered to not vary from place to place.  $\mathbf{P}$ ,  $\mathbf{G}$ ,  $\mathbf{X}$ , and  $\mathbf{B}$  are scalar values and represent absorption coefficients of phytoplankton and



gelbstoff (colored dissolved organic matter plus detritus), backscattering coefficient of suspended particles, and bottom reflectance at a reference wavelength (normally 440 nm), respectively; and  $H$  is the bottom depth. Although multiple bottom types could be incorporated into the semi-analytical model [11, 29], it is only the spectral reflectance shape of a sandy type bottom [11] is considered here as it was the dominant bottom substrate. To derive the five unknowns, a computer module, Hyperspectral Optimization Processing Execution (HOPE), has been developed. By varying the values of the five unknowns, they are considered derived when the modeled  $R_{rs}$  spectrum best matches the Hyperion  $R_{rs}$  spectrum [10, 11]. Unlike traditional empirical algorithms for bathymetry [30-32] that require many assumptions and ground truth data before the derivation of bathymetry from  $R_{rs}$ , HOPE derives all the constituents from the imagery.

## 5 RESULTS AND DISCUSSION

As an example to show the spatial variation of water property of the study area, Figure 4 (left) displays the water's total absorption coefficient at 440 nm ( $a(440)$ , which is the sum of  $P$ ,  $G$  and  $a_w$  at 440 nm) derived from Hyperion imagery, presented prior to geo-referencing (the same for Fig. 5). Pixels of land and deep ocean are masked as white in order to emphasize the properties of optically shallow waters (see Fig. 5). Spatially, we see a contrast of near uniform distribution in the lower half, while a strongly varying distribution in the upper half that is closely associated with land. Lower  $a(440)$  values ( $\sim 0.04 \text{ m}^{-1}$ ) are generally found in the bottom portion of the image while higher values ( $\sim 0.6 \text{ m}^{-1}$ ) are found for waters closer to land. A systematic increase of  $a(440)$  (Note that lower  $a(440)$  indicates higher water clarity.) from offshore to onshore in a pattern parallel to the coastal line is revealed. Such a distribution is expected as the bottom portion is constantly mixing and exchanging waters with the nearby clear oceanic waters by tides and currents (see Fig. 1); whereas the waters with higher  $a(440)$  values are affected by land and river runoff. These spatial variations clearly indicate the different forces (tides, currents, river flows) in modulating optical properties of coastal ecosystem.

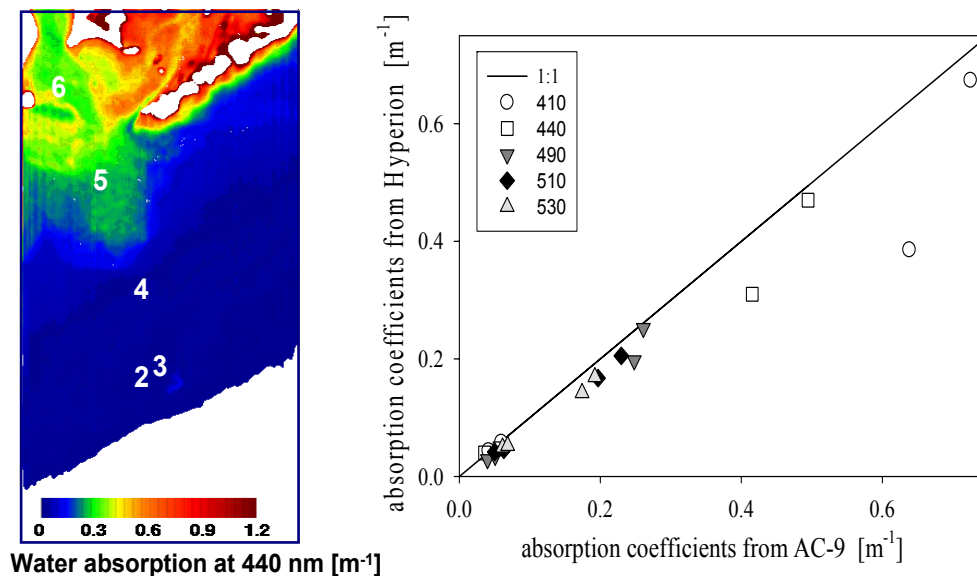


Fig. 4. Left: Distribution (before geo-referencing) of water absorption at 440 nm ( $a(440)$ ) derived from Hyperion data (after  $3 \times 3$  spatial average). Right: Comparison between absorption coefficients from Hyperion and those from AC-9 measurements.

To evaluate the accuracy of optical properties derived from Hyperion imagery, Figure 4 (right) compares Hyperion-derived absorption coefficients at the five blue-green wavelengths (with center wavelengths at the vicinity of 410, 440, 490, 510, and 530 nm) with those measured with an AC-9 instrument (Wetlabs, Inc.). Before matching data from *in situ* measurements, a 3x3 spatial average was carried out to the Hyperion results. For four stations (Sts. 2, 4, 5, and 6) that have high-quality *in situ* absorption measurements (in a range of 0.036 – 0.73 m<sup>-1</sup>), Hyperion results matched *in situ* values very well (average difference is ~ 16.5%). The AC-9 values at St.3 were noisy and therefore excluded in this comparison. Most of the errors (~40% underestimate at 410 nm) happened at St.5 where apparently the water was quite dynamic due to runoff waters. Realizing that absorption coefficients from AC-9 were not error free [33] and the study area was quite complex optically, the relatively small error suggests very successful retrieval of water's total absorption coefficients from Hyperion. No comparisons were made regarding the derived absorption coefficients of phytoplankton pigments or colored dissolved organic matter because there were no *in situ* measurements regarding these properties. It is generally understood, however, that less accurate results are expected from ocean-color remote sensing for the individual components [34].

It is necessary to point out that both Hyperion data and *in situ* measurements showed wide varying (by an order of magnitude) optical properties for such a small area (~ 7 km in width and 20 km in length). If a method to retrieve bottom properties relies on the assumption of homogeneous spatial distribution of water's optical properties, then it will have difficulties for such an area.

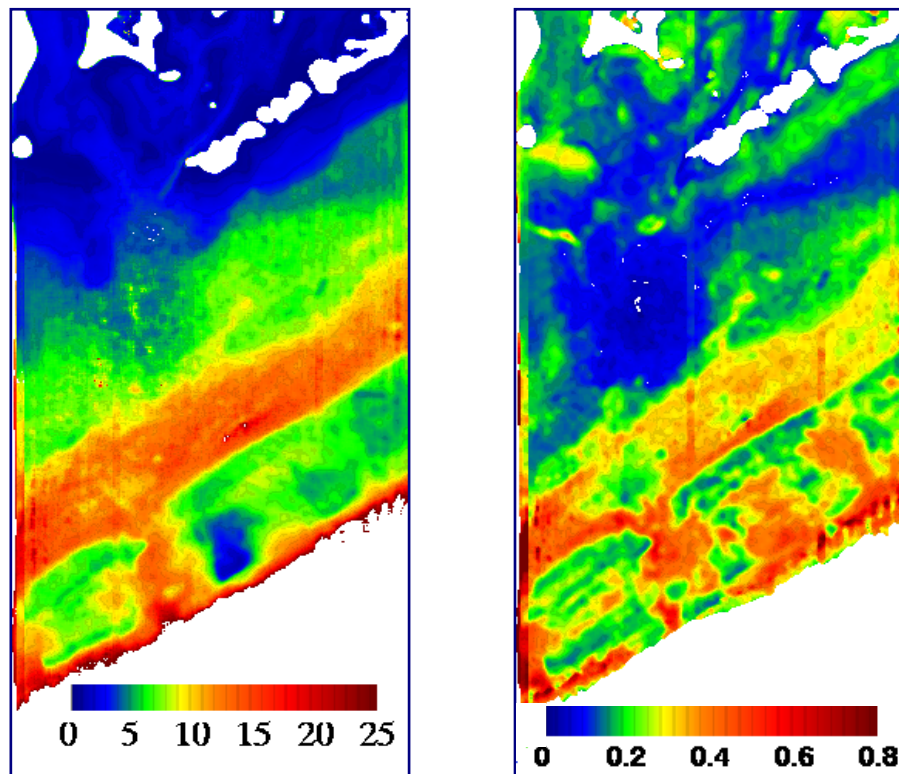


Fig. 5. Distribution (before geo-referencing) of bottom depth (left) and bottom reflectance at 550 nm (right) derived from Hyperion data (after 3x3 spatial average).

In contrast to the spatial patterns of the  $a(440)$  image, the images of bottom depth and bottom reflectance (at 550 nm) from Hyperion show significantly different patterns (Fig. 5). For the lower half of the image where  $a(440)$  is nearly uniform, the bathymetry and bottom reflectance images show distinctive patchiness with wide variations in values. The Hyperion bathymetry shows a variation between  $\sim 1$  and 25 m, with shallow bottoms and a deeper channels clearly revealed (and the ship channel - known as the Hawk channel - parallel to the coast). The bottom reflectance derived from Hyperion image is generally in a range of 0.05 – 0.4, which are reasonable and consistent with mud to quartz sand bottoms (unfortunately we do not have sample measurements to make detailed evaluation). Also, in the middle of the bottom reflectance image, the deposit and accumulation of land runoff is evident. These distinctive patterns and results indicate that properties of bottom and the water column are successfully separated.

To get both qualitative and quantitative evaluations of the bathymetry data derived from the hyperspectral imagery, Hyperion bathymetry is compared with that obtained from the SHOALS system (Fig. 6) after geo-referencing the Hyperion data and binning the LIDAR data (which originally has a spatial resolution of  $\sim 1$  m). Figure 6 shows the spatial distributions of the two bathymetry data sets. Further, using the data in Figure 6, a scatter plot comparing the depths obtained with the LIDAR and Hyperion is presented in Figure 7a; while Figure 7b shows the distribution of relative errors. Clearly, from Figure 6, both bathymetry images show spatial patterns that mimic each other, except for a small portion in the upper middle section (the oval circle) where Hyperion bathymetry is frequently shallower than LIDAR bathymetry. This mismatch may be caused by land runoff that likely produced a two-layer stratified water system. This may result in shallower bathymetry derived from the HOPE processed Hyperion data than is actually present. Combining hyperspectral observation with hydrodynamic models could improve retrievals for such environments, or at least to flag it as an area with likely larger uncertainties.

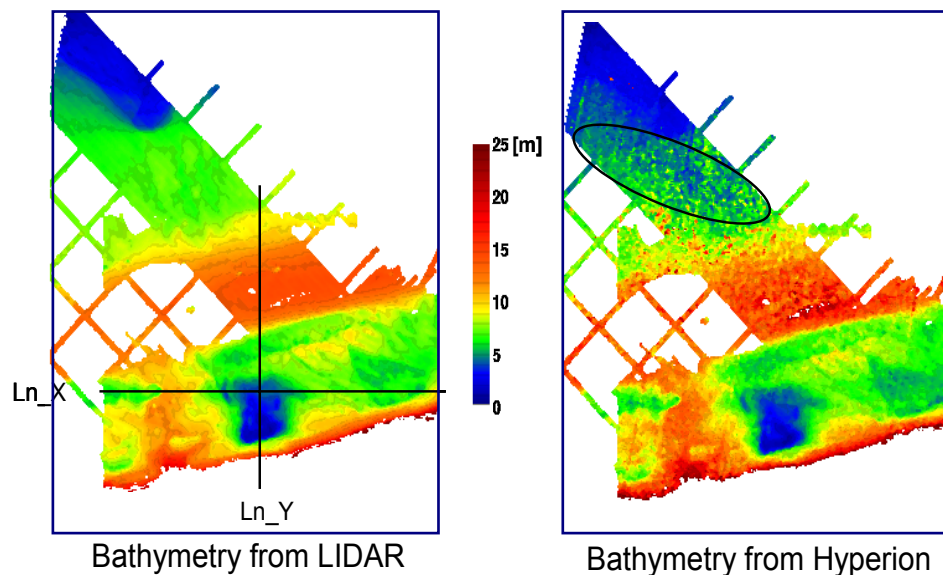


Fig. 6. Left: Bathymetry from LIDAR measurements. Right: Bathymetry from Hyperion data after geo-referencing. Pixels without LIDAR data, and those of land and deep ocean, are masked as white.

Quantitatively, for over 50,000 points that have measurements of bathymetry from both systems and cover a range of ~1 – 25 meters, the two data sets show very good agreement (average percentage difference is ~11%, Figure 7a). Overall 58% of the Hyperion bathymetry are within  $\pm 10\%$  of LIDAR bathymetry (Figure 7b). This percentage becomes 76% if the difference is expanded to  $\pm 15\%$  and 84% for  $\pm 20\%$ . All these results indicate excellent bathymetry retrieval from this Hyperion imagery using the HOPE scheme.

The reason for larger (~20%) overestimation at the locations where the Hyperion bathymetry is greater than 20 m (~2% of data points, Figure 7a) is as yet unknown. It is noticed, however, that 90% of such data points (Hyperion-derived bathymetry deeper than 20 m) occur at the lower boundary between shallow coastal water and deeper oceanic water where bathymetry increases dramatically. Because the spatial resolution of Hyperion is ~30 m, the Hyperion signals of pixels in the boundary area are a mixture of shallow and deep water, and therefore result in a deeper depth retrieval than is actually present. Fortunately such pixels can be easily identified in an image and can be flagged.

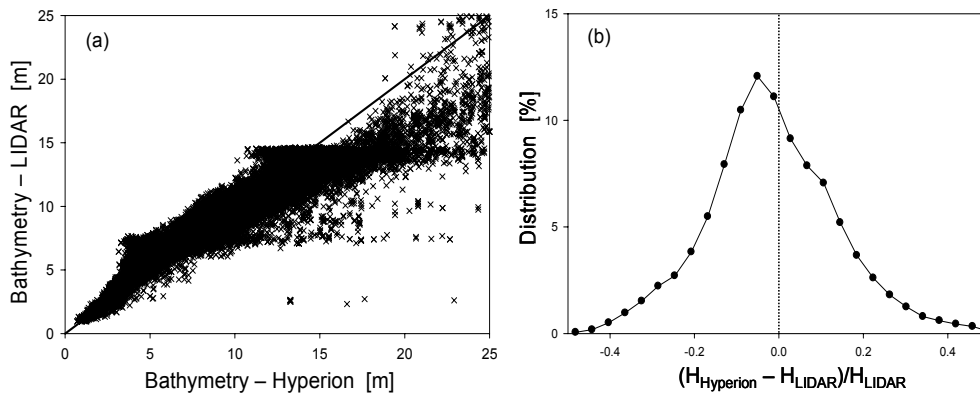


Fig. 7. (a) Quantitative comparison between Hyperion bathymetry and LIDAR bathymetry. (b) Distribution of relative error when Hyperion bathymetry is compared with LIDAR bathymetry.

To compare the two bathymetry data in detail, Figure 8 presents the bathymetry tracks for the two transects (black lines) in Figure 6, respectively. These two transects cover wide variations of bathymetry in the horizontal and vertical directions. Though we do observe some mismatches in bathymetry values, overall there is excellent agreement both in patterns and in actual values between the two independently determined bathymetry data sets. All these results, both water column and bottom properties, indicate successful derivation of environmental properties from hyperspectral imagery with the approaches used in this study. These results echo the findings of Brando and Dekker [7] that Hyperion imagery is very useful to observe environmental properties of complex coastal ecosystems.

## 6 SUMMARY AND CONCLUSIONS

In this study, using Hyperion data over Looe Key as an example, we demonstrate an innovative approach to derive high-quality spectral  $R_{rs}$  of the water from Hyperion imagery. This new method uses differences in scene brightness to avoid the rigid requirement of accurate radiometric calibration of the sensor, and overcomes the commonly encountered problem of negative  $R_{rs}$  in the blue wavelengths when using the standard atmosphere correction scheme. The limitation of this new method is that it requires distinctive cloud shadow in a near uniform water area.

The  $R_{rs}$  derived from Hyperion imagery was applied to a previously developed hyperspectral retrieval scheme to obtain properties of the water column, bottom reflectance, and bottom depth. The derived absorption coefficients differ on average by  $\sim 16.5\%$  when compared with that measured *in situ* (over a range of  $0.036 - 0.73 \text{ m}^{-1}$  for wavelengths of 410, 440, 490, 510, and 530 nm); while the derived bathymetry differs on average by just  $\sim 11\%$  when compared with that from LIDAR measurements (over a range of  $\sim 1 - 25 \text{ m}$ ). Comparisons show that 76% of the Hyperion bathymetry values are within  $\pm 15\%$  of the LIDAR bathymetry; and 84% are within  $\pm 20\%$ . These results suggest excellent retrieval of bathymetry from a space-borne hyperspectral imager (Hyperion). A key feature of this study is that the entire top-down process of the image did not use (or need) *a priori* or *in situ* information. The derived results of water column and bottom demonstrate further that, despite its limited SNR and radiometric accuracy, Hyperion imagery is quite adequate for observation and monitoring of bright coastal environments providing that sophisticated and robust algorithms are implemented.

Given the importance of the coastal ecosystems for life quality and the global climate, efficient and adequate information about the biogeochemical contents, water clarity, bathymetry, and distribution of benthic habitats of coastal ecosystems is important for government agencies and the public. There is an important but unmet need for regularly updating our knowledge about the coastal environment and identifying locations of dramatic change. The results of this study, and the many others, show the capability and usefulness of hyperspectral sensors in monitoring coastal ecosystems [4]. Unfortunately, no such space-borne sensors are in operational status yet, even though Hyperion is presently in orbit. The MERIS satellite sensor of ESA, though not ideal in spatial and spectral configurations desired for coastal remote sensing, does have 15 spectral bands covering the visible to infrared domain and capable to collect data with a 300 m spatial resolution. Before an operational satellite sensor with ideal spatial and spectral configurations is available, MERIS data, as recently shown in Lee et al. [35], could be used as a surrogate for routine, though relatively coarse, observations of many coastal environments.

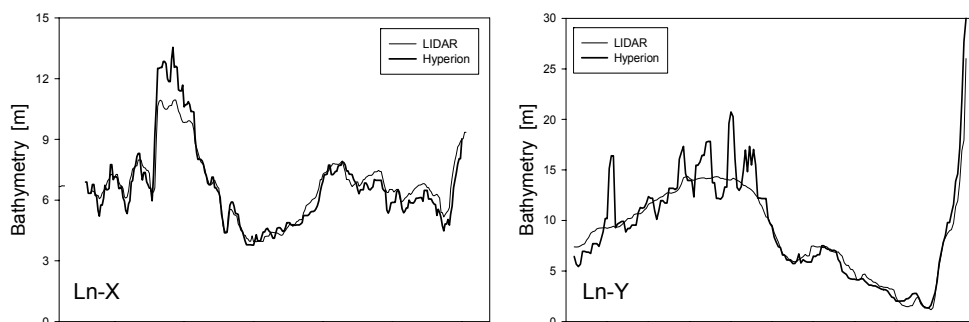


Fig. 8. Detailed bathymetry comparison between Hyperion data and LIDAR data for the two transects (Ln\_X and Ln\_Y) in Fig. 6.

## Acknowledgments

Support for this study was provided by NASA through the “Evaluation of EO-1 Hyperion and ALI data for coastal waters” project and NRL through the “Lidar and Hyperspectral Remote Sensing of Littoral Environment (NRL 73-6734)” project. We also thank Todd Taylor at SAIC in helping EO-1 data acquisition and NOAA for the collection and archive of the EO-1 data. Comments and suggestions from two anonymous reviewers are gratefully acknowledged.

## References

- [1] S. L. Miller and M. P. Crosby, "The extent and condition of US Coral Reefs," NOAA's State of the Coast Report, Silver Spring, MD (1998).
- [2] M. O. Hall, M. D. Durako, J. W. Fourqurean, and J. C. Zieman, "Decadal scale changes in seagrass distribution and abundance in Florida Bay," *Estuaries* **22**, 445-459 (1999) [doi:10.2307/1353210].
- [3] IOCCG, "Remote Sensing of Ocean Colour in Coastal, and Other Optically-Complex, Waters," in *Reports of the International Ocean-Colour Coordinating Group, No. 3*, S. Sathyendranath, Ed. Dartmouth, Canada: IOCCG (2000).
- [4] C. O. Davis, K. L. Carder, B.-C. Gao, Z. P. Lee, and W. P. Bissett, "The Development of Imaging Spectrometry of the Coastal Ocean," in *Proc. IEEE Int. Geosci. Rem. Sens. Symp.*, 1982-1985 (2006) [doi: 10.1109/IGARSS.2006.513].
- [5] Z. P. Lee and K. L. Carder, "Effect of spectral band numbers on the retrieval of water column and bottom properties from ocean color data," *Appl. Opt.* **41**, 2191-2201, (2002) [doi:10.1364/AO.41.002191].
- [6] S. G. Ungar, "Overview of the Earth Observing One (EO-1) Mission," *IEEE Trans. Geosci. Rem. Sens.* **41**(6), 1149-1159 (2003) [doi: 10.1109/TGRS.2003.815999].
- [7] V. E. Brando and A. G. Dekker, "Satellite hyperspectral remote sensing for estimating estuarine and coastal water quality," *IEEE Trans. Geosci. Rem. Sens.* **41**, 1378-1387 (2003) [doi:10.1109/TGRS.2003.812907].
- [8] P. Barry, P. Jarecke, J. Pearlman, D. Jupp, J. Lovell, and S. Campbell, "Radiometric calibration validation of the Hyperion instrument using ground truth at a site in Lake Frome, Australia," in *Imaging Spectrometry VII*, M. R. Descour and S. S. Shen, Eds., *Proc. SPIE* **4480**, 242-246 (2002) [doi: 10.1117/12.453346].
- [9] H. R. Gordon and M. Wang, "Retrieval of water-leaving radiance and aerosol optical thickness over oceans with SeaWiFS: A preliminary algorithm," *Appl. Opt.* **33**, 443-452 (1994).
- [10] Z. P. Lee, K. L. Carder, C. D. Mobley, R. G. Steward, and J. S. Patch, "Hyperspectral remote sensing for shallow waters: 2. Deriving bottom depths and water properties by optimization," *Appl. Opt.* **38**, 3831-3843 (1999).
- [11] Z. P. Lee, K. L. Carder, R. F. Chen, and T. G. Peacock, "Properties of the water column and bottom derived from AVIRIS data," *J. Geophys. Res.* **106**, 11639-11652 (2001) [doi:10.1029/2000JC000554].
- [12] R. G. Steward, K. L. Carder, and T. G. Peacock, "High resolution in water optical spectrometry using the Submersible upwelling and downwelling spectrometer (SUDS)," in *EOS AGU-ASLO*, San Diego, CA (1994).
- [13] J. L. Mueller, G. S. Fargion, and C. R. McClain, "Ocean Optics Protocols For Satellite Ocean Color Sensor Validation, **Revision 4**," Goddard Space Flight Center, Greenbelt, MD (2003).
- [14] H. R. Gordon, "Removal of atmospheric effects from satellite imagery of the oceans," *Appl. Opt.* **17**, 1631-1636 (1978).
- [15] B. C. Gao, M. J. Montes, Z. Ahmad, and C. O. Davis, "Atmospheric correction algorithm for hyperspectral remote sensing of ocean color from space," *Appl. Opt.* **39**, 887-896 (2000).
- [16] P. Reinersman, K. L. Carder, and F. R. Chen, "Satellite-sensor calibration verification with the cloud-shadow method," *Appl. Opt.* **37**, 5541-5549 (1998).
- [17] W. W. Gregg and K. L. Carder, "A simple spectral solar irradiance model for cloudless maritime atmospheres," *Limnol. Oceanogr.* **35**, 1657-1675 (1990).
- [18] Z. P. Lee, K. L. Carder, C. D. Mobley, R. G. Steward, and J. S. Patch, "Hyperspectral remote sensing for shallow waters. 1. A semianalytical model," *Appl. Opt.* **37**, 6329-6338 (1998).

- [19] J. T. O. Kirk, "Volume scattering function, average cosines, and the underwater light field," *Limnol. Oceanogr.* **36**, 455-467 (1991).
- [20] A. Morel and B. Gentili, "Diffuse reflectance of oceanic waters (2): Bi-directional aspects," *Appl. Opt.* **32**, 6864-6879 (1993).
- [21] Z. P. Lee, K. L. Carder, and K. P. Du, "Effects of molecular and particle scatterings on model parameters for remote-sensing reflectance," *Appl. Opt.* **43**, 4957-4964 (2004) [doi:10.1364/AO.43.004957].
- [22] J. D. Hedley, A. R. Harborne, and P. J. Mumby, "Simple and robust removal of sun glint for mapping shallow-water benthos," *Int. J. Rem. Sens.* **26**, 2107-2112 (2005) [doi:10.1080/01431160500034086].
- [23] S. Asano, M. Shiobara, Y. Nakanishi, and Y. Miyake, "A multichannel cloud pyranometer system for airborne measurement of solar spectral reflectance by clouds," *J. Atmos. Ocean. Tech.* **12**, 479-487 (1995) [doi:10.1175/1520-0426].
- [24] M. D. King, W. P. Menzel, P. S. Grant, J. S. Myers, G. T. Arnold, S. E. Platnick, L. E. Gumley, S.-C. Tsay, C. C. Moeller, M. Fitzgerald, K. S. Brown, and F. G. Osterwischg, "Airborne scanning spectrometer for remote sensing of cloud, aerosol, water vapor, and surface properties," *J. Atmos. Ocean. Tech.* **13**, 777-794 (1996) [doi:10.1175/1520-0426].
- [25] H. R. Gordon and D. K. Clark, "Clear water radiances for atmospheric correction of coastal zone color scanner imagery," *Appl. Opt.* **20**, 4175-4180 (1981).
- [26] J. L. Mueller, C. Davis, R. Arnone, R. Frouin, K. L. Carder, Z. P. Lee, R. G. Steward, S. Hooker, C. D. Mobley, and S. McLean, "Above-water radiance and remote sensing reflectance measurement and analysis protocols," in *Ocean Optics Protocols for Satellite Ocean Color Sensor Validation, Revision 3*, J. L. Mueller and G. S. Fargion, Eds., *NASA/TM-2002-210004*, 171-182 (2002).
- [27] R. Pope and E. Fry, "Absorption spectrum (380 - 700 nm) of pure waters: II. Integrating cavity measurements," *Appl. Opt.* **36**, 8710-8723 (1997).
- [28] A. Morel, "Optical properties of pure water and pure sea water," in *Optical Aspects of Oceanography*, pp. 1-24, N. G. Jerlov, and E. S. Nielsen, Eds., Academic, New York, (1974).
- [29] C. D. Mobley, L. K. Sundman, C. O. Davis, J. H. Bowles, T. V. Downes, R. A. Leathers, M. J. Montes, W. P. Bissett, D. D. R. Kohler, R. P. Reid, E. M. Louchard, and A. Gleason, "Interpretation of hyperspectral remote-sensing imagery by spectrum matching and look-up tables," *Appl. Opt.* **44**, 3576-3592 (2005) [doi:10.1364/AO.44.003576].
- [30] R. K. Clark, T. H. Fay, and C. L. Walker, "Bathymetry calculations with Landsat 4 TM imagery under a generalized ratio assumption," *Appl. Opt.* **26**, 4036-4038, (1987).
- [31] D. R. Lyzenga, "Shallow-water bathymetry using combined lidar and passive multispectral scanner data," *Int. J. Rem. Sens.* **6**, 115-125 (1985) [doi:10.1080/01431168508948428].
- [32] R. P. Stumpf, K. Holderied, and M. Sinclair, "Determination of water depth with high-resolution satellite imagery over variable bottom types," *Limnol. Oceanogr.* **48**, 547-556 (2003).
- [33] W. S. Pegau, J. S. Cleveland, W. Doss, C. D. Kennedy, R. A. Maffione, J. L. Mueller, R. Stone, C. C. Trees, A. D. Weidemann, W. H. Wells, and J. R. V. Zaneveld, "A comparison of methods for the measurement of the absorption coefficient in natural waters," *J. Geophys. Res.* **100**, 13201-13220 (1995) [doi:10.1029/95JC00456].
- [34] IOCCG, "Remote sensing of inherent optical properties: fundamentals, tests of algorithms, and applications," in *Reports of the International Ocean-Colour Coordinating Group, No. 5*, Z.-P. Lee, Ed. (2006).
- [35] Z. P. Lee, C. Hu, D. Gray, B. Casey, R. Arnone, A. Weidemann, R. Ray, and W. Goode, "Properties of coastal waters around the US: Preliminary results using MERIS

data," in *ENVISAT Symp.*, Montreux, Switzerland (2007).